ADVANCING EARTH AND SPACE SCIENCES

JGR Oceans

RESEARCH ARTICLE
10.1029/2024JC022062

**Key Points:**

- Conductive heat flux (CHF) over ice-covered areas of the Arctic Ocean increases from 1979 to 2022
- CHF changes are apportioned to components due to changes in ice thickness, snow depth, and surface skin temperature
- Magnitude of the CHF changes are comparable to those in surface sensible heat flux, latent heat flux, and net radiation flux

**Correspondence to:**
Y. Liu,
yinghui.liu@noaa.gov

**Citation:**
Liu, Y., & Zhang, J. (2025). Conductive heat flux over Arctic sea ice from 1979 to 2022. *Journal of Geophysical Research: Oceans*, *130*, e2024JC022062. https://doi.org/10.1029/2024JC022062

Received 1 NOV 2024
Accepted 24 JUN 2025

**Author Contributions:**
**Conceptualization:** Yinghui Liu
**Data curation:** Yinghui Liu, Jinlun Zhang
**Formal analysis:** Yinghui Liu
**Investigation:** Yinghui Liu
**Methodology:** Yinghui Liu
**Validation:** Yinghui Liu
**Visualization:** Yinghui Liu
**Writing – original draft:** Yinghui Liu
**Writing – review & editing:** Yinghui Liu, Jinlun Zhang



# Conductive Heat Flux Over Arctic Sea Ice From 1979 to 2022

**Yinghui Liu[1] and Jinlun Zhang[2]**

[1]Center for Satellite Applications and Research, NOAA/NESDIS, Madison, WI, USA, [2]Polar Science Center, University of Washington, Seattle, WI, USA

**Abstract** The conductive heat flux (CHF) from the ocean to the snow/sea ice-atmosphere interface through sea ice is a crucial component of the surface energy budget over the sea ice-covered Arctic Ocean. The CHF is influenced by surface skin temperature, sea ice thickness, and depth of snow on sea ice. This study uses monthly mean surface skin temperature from ERA5 reanalysis, and sea ice thickness and snow depth from the Pan-Arctic Ice-Ocean Modeling and Assimilation System to derive the means and changes of CHF over the Arctic Ocean from 1979 to 2022. The findings reveal that CHFs are generally positive (from flux to the surface from below) from November to March and negative from June to August. CHFs are large in peripheral seas with thin sea ice and low snow depth, and small over pack ice with thick sea ice and snow. The thinning of sea ice and snow on sea ice contributes to increasing CHF, while rising surface skin temperatures lead to decreasing CHF. Overall, CHF increases from 1979 to 2022, primarily driven by the thinning of sea ice. The magnitude of CHF changes during this period is comparable to or higher than those in sensible heat flux, latent heat flux, and net longwave/thermal radiation flux at the surface from November to March over the peripheral seas. A better representation of sea ice thickness and snow depth over sea ice in the reanalysis would possibly improve the depiction of CHF and surface temperature changes.

**Plain Language Summary** Conductive heat flux (CHF) in the Arctic Ocean describes how heat moves from the ocean through sea ice to the ice/snow surface. It is influenced by surface temperature, sea ice thickness, and snow depth. This study used monthly average surface skin temperature data from ERA5 reanalysis and sea ice thickness/snow depth data from Pan-Arctic Ice-Ocean Modeling and Assimilation System reanalysis to analyze CHF means and changes from 1979 to 2022. CHF tends to be positive (heat moving upward) from November to March and negative from June to August. Its higher in peripheral seas where sea ice is thin and snow depth is low, and lower in areas with thicker sea ice and snow cover. Thinning sea ice and snow contribute to increasing CHF, while warmer surface temperatures lead to decreasing CHF. Overall, CHF increases during this period are mainly due to sea ice thinning. The changes in CHF in magnitude are comparable to or higher than changes in sensible heat flux, latent heat flux, and net longwave/thermal radiation flux at the surface.

## 1. Introduction

The Arctic region has experienced dramatic changes over the past several decades, evidenced by variations in surface temperature, sea ice, and snow on sea ice, among many other parameters and processes. The Arctic surface has warmed at a rate more than twice that of the global average (Serreze et al., 2009; P. C. Taylor et al., 2022). This phenomenon, known as Arctic amplification or polar amplification, is observed in surface skin temperature and air temperature from both observations and climate models (Chylek et al., 2022; Moon et al., 2023; Rantanen et al., 2022; P. C. Taylor et al., 2022). Multiyear sea ice, which survives at least one summer, is generally thicker than first-year sea ice because it is through a longer period of growth. However, multiyear sea ice has increasingly been replaced by first-year sea ice over the Arctic Ocean (J. A. Maslanik et al., 2007, J. Maslanik et al., 2011), with a decrease in the mean sea ice thickness over the past few decades (Kwok, 2018; Liu et al., 2020; Moon et al., 2023). Although there is considerable uncertainty in the estimation of snow depth over sea ice (Lawrence et al., 2018; Shalina & Sandven, 2018), studies have shown geography-dependent snow depth trends (Lee et al., 2021) and snow depth reduction over sea ice in recent decades (Webster et al., 2014).

Over the sea ice-covered Arctic Ocean, conductive heat flows from the warmer ocean through the sea ice to the colder snow/ice and the atmosphere interface for most of the year. This conductive heat flux (CHF) is a component of the surface energy budget over the Arctic Ocean and a factor that can influence the ice surface temperature. The CHF is also closely related to sea ice growth, as the latent heat of fusion during ice growth is a source of the CHF. Studying the CHF helps in understanding changes in surface temperature and sea ice thickness in the Arctic over the last several decades. Direct measurements of the CHF through sea ice have been made but with very limited spatial representativeness (Webster et al., 2014). The CHFs are often parameterized as a function of sea ice thickness, snow depth over sea ice, and surface skin temperature (Landrum & Holland, 2022; Wang et al., 2010). As the entire Arctic climate system evolves, the changes in sea ice thickness, snow depth, and sea ice skin temperature over the Arctic Ocean in the past few decades likely involve changes in every energy budget component at the surface, including the CHF.

Landrum and Holland (2022) investigated the influence of changes in sea ice and snow thickness on simulated Arctic winter CHFs from 1950 to 2070 based on simulations from the Community Earth System Model version 1 Large Ensemble. They found an increase of approximately 7–11 $\mathrm{Wm^{-2}}$ in wintertime CHFs over the ice-covered Arctic Ocean by the mid-21st century, with changes in both sea ice thickness and snow thickness being important contributors to these changes in CHFs. Global climate models (GCMs) tend to have large uncertainties in simulating sea ice thickness and snow depth over sea ice. Besides GCM simulations, a few ice thickness data sets are available, including ice thickness estimations from sea ice freeboard observations using space-based lidar and radar altimeters from the early 2000s to the present (Connor et al., 2009; Kwok & Rothrock, 2009; Laxon et al., 2013), passive visible and infrared radiometers using the one-dimensional thermodynamic ice model from 1982 to the present (Wang et al., 2010), and the Pan-Arctic Ice-Ocean Modeling and Assimilation System (PIOMAS) from 1979 to the present (Schweiger et al., 2011). Furthermore, PIOMAS also provides snow depth over sea ice. These data sets mentioned above make it possible to study the CHF over the ice-covered Arctic Ocean.

This study presents the means and changes of CHF in the Arctic from 1979 to 2022 based on sea ice thickness and snow depth from the PIOMAS reanalysis and surface skin temperature from the ERA5 reanalysis. The partition of the overall CHF changes into components due to changes in sea ice thickness, snow depth, and surface skin temperature is analyzed. This study, using reanalysis products, serves as a complement to the work of Landrum and Holland (2022). Because of data assimilation, these reanalysis products have lower uncertainties than those of GCM models, thus likely providing more realistic details in the CHF means and changes from 1979 to 2022. In this study, we also compared the derived CHF with other surface energy flux terms to reveal the relative importance of CHF over the sea ice-covered areas of the Arctic Ocean, and its contribution to the Arctic amplification.

## 2. Materials and Methods

### 2.1. Methods

Following Semtner (1976) and Landrum and Holland (2022), with an assumption of linear vertical temperature distribution inside the snow and sea ice, CHF is estimated with the following equation:

$$\mathrm{CHF} = \frac{K_i K_s (T_f - T_s)}{K_s h_i + K_i h_s} \tag{1}$$

where $K_s$ (0.31 $\mathrm{Wm^{-1}K^{-1}}$) and $K_i$ (2.0 $\mathrm{Wm^{-1}K^{-1}}$) are the snow and ice conductivities of heat, respectively, $h_s$ and $h_i$ are snow depth and sea ice thickness in meters, and $T_f$ and $T_s$ are temperatures at ocean-ice and ice/snow-atmosphere interfaces, respectively. $T_f$ is a function of ocean water salinity, $-0.0592\mathrm{S}$-$9.37 \times 10^{-6}\mathrm{S}^2 - 5.33 \times 10^{-7}\mathrm{S}^3$ with S being the ocean water salinity (Notz, 2005). In this study, $T_\mathrm{f}$ is set as a constant 271.15 K with a constant ocean water salinity of 33 ppt (Anheuser et al., 2022). Positive CHF indicates heat flux flows from the ocean through sea ice to the snow/ice-atmosphere interface, and vice versa. In this study, the CHF is only calculated over regions with sea ice concentrations equal to or higher than 80%.

Monthly CHFs from 1979 to 2022 over the Arctic Ocean were calculated using monthly mean sea ice thickness, snow depth, and surface skin temperature. Trends of monthly mean parameters, including CHFs, sea ice thickness, snow depth, and surface skin temperature, from 1979 to 2022 were calculated using linear regression. Confidence levels of the linear trends were calculated using a two-tailed Student's t test. Mean of monthly CHFs, sea ice thickness, snow depth, and surface skin temperature were also calculated.

According to Equation 1, the CHF is a function of sea ice thickness, snow depth over sea ice, and surface skin temperature. The CHF changes or trends can be partitioned into three components that can be attributed to changes in sea ice thickness, snow depth, and surface skin temperature, respectively as follows:

$$\frac{d\mathrm{CHF}}{dt} = \mathrm{Comp1} + \mathrm{Comp2} + \mathrm{Comp3} \tag{2}$$

where Comp1, Comp2, and Comp3 are functions of changes in sea ice thickness, snow depth, and surface skin temperature, respectively, with the assumption that these three components—changes in sea ice thickness, snow depth over sea ice, and surface skin temperature—are independent.

$$\mathrm{Comp1} = -\frac{K_i K_s^2 (T_f - T_s)}{(K_s h_i + K_i h_s)^2} \times \frac{dh_i}{dt} = A \times \frac{dh_i}{dt} \tag{3}$$

$$\mathrm{Comp2} = -\frac{K_i^2 K_s (T_f - T_s)}{(K_s h_i + K_i h_s)^2} \times \frac{dh_s}{dt} = B \times \frac{dh_s}{dt} \tag{4}$$

$$\mathrm{Comp3} = -\frac{K_i K_s}{K_s h_i + K_i h_s} \times \frac{dT_s}{dt} = C \times \frac{dT_s}{dt} \tag{5}$$

Considering the different values of Ks and Ki, the same trend of snow depth leads to a CHF trend ~6.5 times as large as that of the CHF trend from a trend in sea thickness. For a case of sea ice thickness of 2.0 m, snow depth of 0.2 m, and surface skin temperature of 251.0 K, the CHF is 12.2 $\mathrm{Wm}^{-2}$, and the CHF trend dependence on changes in sea thickness, snow depth, and surface skin temperature changes, represented by A, B, and C, respectively, are $-3.7\ \mathrm{Wm}^{-2}/\mathrm{m}$, $-23.8\ \mathrm{Wm}^{-2}/\mathrm{m}$, and $-0.6\ \mathrm{Wm}^{-2}/\mathrm{K}$ respectively.

The correlations between sea ice thickness, snow depth, and surface temperature changes are non-negligible over the Arctic Ocean. Surface temperature and snow depth influence conductive heat flux, which in turn regulates sea ice growth and thickness (Thorndike, 1992; Wang et al., 2010). Both sea ice and overlying snow affect the transfer of heat from the warmer ocean to the surface by acting as thermal insulators (Arduini et al., 2022). Consequently, variations in snow depth and sea ice thickness are likely to impact surface temperature. Research has shown that increased snow accumulation on sea ice can lead to thicker ice cover (Holland et al., 2021). Figure A1 shows significant positive correlations between changes in sea ice thickness and snow depth and negative correlations between changes in surface skin temperature and both sea ice thickness and snow depth changes. If the correlations between sea ice thickness, snow depth, and surface temperature changes are considered, the Comp1, Comp2, and Comp3 are

$$\mathrm{Comp1} = \left(A + B \times \frac{\partial h_s}{\partial h_i} + C \times \frac{\partial T_s}{\partial h_i}\right) \times \frac{dh_i}{dt} \tag{6}$$

$$\mathrm{Comp2} = \left(A \times \frac{\partial h_i}{\partial h_s} + B + C \times \frac{\partial T_s}{\partial h_s}\right) \times \frac{dh_s}{dt} \tag{7}$$

$$\mathrm{Comp3} = \left(A \times \frac{\partial h_i}{\partial T_s} + B \times \frac{\partial h_s}{\partial T_s} + C\right) \times \frac{dT_s}{dt} \tag{8}$$

where the partial derivatives of two variables are calculated as the regression coefficients of these two parameters, for example, $\partial(h_s)/\partial(h_i)$ as the regression coefficient of snow depth and sea ice thickness.

The Arctic Ocean is divided into three regions, region 1 (R1), region 2 (R2), and region 3 (R3) (Figure 1), to investigate how the variables vary across different areas of the Arctic Ocean. These regions were classified based on the spatial distribution of monthly mean PIOMAS sea ice thickness in October from 1979 to 2022. R1 represents the pack ice area with the thickest and mostly perennial sea ice with ice thickness equal to or thicker than 2.2 m; R3 represents the peripheral seas where sea ice is thinnest and seasonal with ice thickness less than 0.8 m; and R2 lies between R1 and R3 and represents the transitional region. These regions are slightly different based on monthly mean PIOMAS sea ice thickness in other months with different thresholds. The R3 does not include all

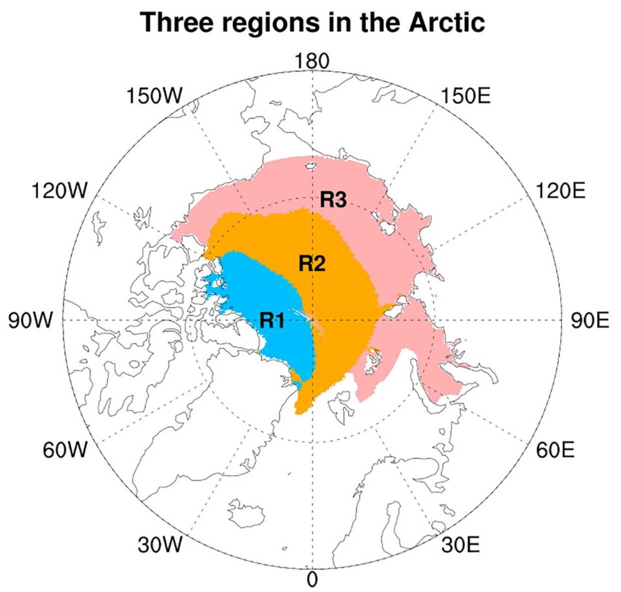


**Figure 1.** Three representative regions in the Arctic. R1: the region with mostly perennial/thick sea ice; R2: transition zone from the perennial/thick sea ice region to the seasonal/thin sea ice region; and R3: the seasonal/thin sea ice region.

the peripheral seas. Variables were averaged over these regions and are shown when over 50% of the regions have valid values, that is, ice covered.

The surface energy budget (SEB) at the surface is presented as

$$SEB = SSR + STR + SSHF + SLHF + CHF + RES \quad (9)$$

where SSR is the surface net solar radiation flux, the surface net longwave radiation flux (STR) is the total of surface downward longwave radiation flux (STRD) and surface upward longwave radiation flux; SSHF and SLHF are surface sensible heat flux and surface latent heat flux, respectively; and RES is the residual heat flux. When we compared the derived CHF with other surface energy flux terms over the sea ice-covered areas of the Arctic Ocean, our main focus was in wintertime; thus, the SSR term was not included.

### 2.2. Data

The monthly mean sea ice thickness and snow depth from 1979 to 2022 come from PIOMAS reanalysis. PIOMAS is a coupled ice-ocean model, which consists of a 12-category thickness and an enthalpy-distribution sea ice model and the Parallel Ocean Program (Schweiger et al., 2011; Zhang & Rothrock, 2001, 2003). A snow model in terms of snow thickness distribution corresponding to the ice thickness distribution accompanies the sea ice model. The sea ice thickness and snow depth are derived from jointly solving the thickness-distribution equations of sea ice thickness and snow depth and an enthalpy-distribution equation. PIOMAS uses daily mean NCEP/NCAR reanalysis data as atmospheric forcing, and assimilates daily satellite derived sea ice concentration and sea surface temperature (Lindsay & Zhang, 2006; Schweiger et al., 2011).

Monthly mean surface skin temperature from 1979 to 2022 comes from ERA5 reanalysis (Hersbach et al., 2020). Other monthly mean parameters 1979 to 2022 from ERA5 reanalysis were also used in this study. They include surface sensible heat flux, latent heat flux, downward longwave radiation flux at the surface, and net longwave/thermal radiation flux at the surface.

## 3. Results

The high CHF values generally correspond to the low values in sea ice thickness, snow depth, and skin temperature, and vice versa. Figure 2 shows an example of derived CHF in January 2001, based on monthly mean sea ice thickness, snow depth over sea ice, and surface skin temperature, as per Equation 1. The derived CHF exhibits a pattern of higher values over peripheral seas, with the maximum CHF of over 18.0 $Wm^{-2}$ observed in the coastal areas of the Kara and Barents Seas, and lower values of less than 12.0 $Wm^{-2}$ over pack ice areas north of the Canadian Archipelago and Greenland. The sea ice is thickest north of the Canadian Archipelago and becomes thinner toward the peripheral seas, with the thinnest sea ice over the Kara and Barents Seas. The snow depth follows a similar spatial pattern to that of ice thickness, except that snow depth is more spatially heterogeneous. Surface skin temperature often has similar spatial patterns to sea ice thickness and snow depth, with the coldest temperatures over thick ice and warmer temperatures over peripheral seas. In January 2001, there was an extended low-temperature area from the Canadian Archipelago to East Siberia.

The mean monthly CHFs from 1979 to 2022 over the Arctic Ocean are depicted in Figure 3. Spatially, the largest CHFs occur near the coastal areas and peripheral seas, where minimum sea ice thickness, snow depth, and warmest surface temperatures exist. Toward the perennial ice, the CHF decreases and reaches a minimum in the regions north of the Canadian Archipelago and Greenland, where the thickest sea ice and snow depth, along with the lowest surface temperature, prevail. Seasonally, the maximum positive CHFs of over 24.0 $Wm^{-2}$ appear in November and December, especially over the peripheral seas during the sea ice growth phase. From January to May, the CHF gradually decreases as sea ice thickness and snow depth increase. It then becomes negative from June to August when the sea ice and snow start to melt, with skin temperatures exceeding the freezing point. Finally, the CHF returns to positive values in September and continues to increase thereafter.

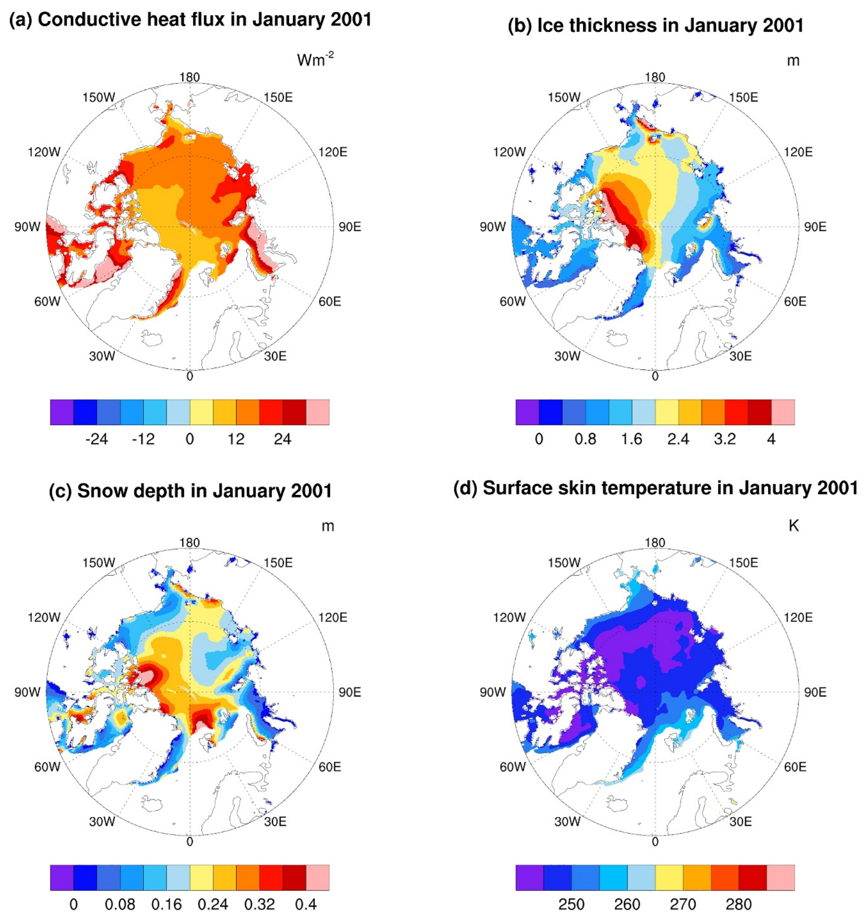


**Figure 2.** (a) Derived conductive heat flux ($Wm^{-2}$), (b) ice thickness (m), (c) snow depth (m), and (d) surface skin temperature (K) monthly means in January 2001.

The annual cycles of monthly mean CHFs, sea ice thickness, snow depth, and surface skin temperature averaged over regions R1, R2, R3, and the whole Arctic Ocean, respectively, are illustrated in Figure 4. Over R1, R2, and R3, sea ice begins to grow in September or October, reaches its maximum thickness in May, and subsequently melts, consistent with findings in Liu et al. (2020). This feature is not seen in the monthly mean ice thickness over all regions, because all regions include R3 from June to October, when the sea ice thickness at its minimum over R3. Snow depth increases from August and starts decreasing in May. Surface skin temperature is warmest and above the freezing point from June to August, and then gradually cools, reaching its lowest point in February. Notably, sea ice is thickest over R1 and thinnest over R3 throughout the year, mirroring the snow depth patterns. Additionally, surface skin temperature is warmest over R3 and coldest over R1. The derived CHFs exhibit their highest positive values in November and December across all regions—over 20.0, 15.0, and 10.0 $Wm^{-2}$ for R3, R2, and R1, respectively. These values remain higher than 10.0 $Wm^{-2}$ over R1 and R2 from January to March, decrease thereafter, become negative from June to August, and then return to positive in September. Overall, the highest CHFs occur over R3, while the lowest are observed over R1. These annual cycles align with the features depicted in Figure 3.

Changes of monthly CHFs from January to December spanning the years 1979–2022 are illustrated in Figure 5, with time series of monthly mean CHFs in November to February from 1979 to 2022 over region R1, R2, and R3 and over all regions in Figure 6. The changes are predominantly positive over the Arctic Ocean between October and March, with negative values observed in June and August. The most significant increasing changes of over 0.24, 0.24, and 0.16 $Wm^{-2}$/year are observed over the Beaufort, Chukchi, and East Siberian Seas in November, December, and January, respectively, corresponding to peak mean CHFs during those months, and smaller positive changes of less than 0.16 $Wm^{-2}$/year over the pack ice. These features are consistent with the CHF time

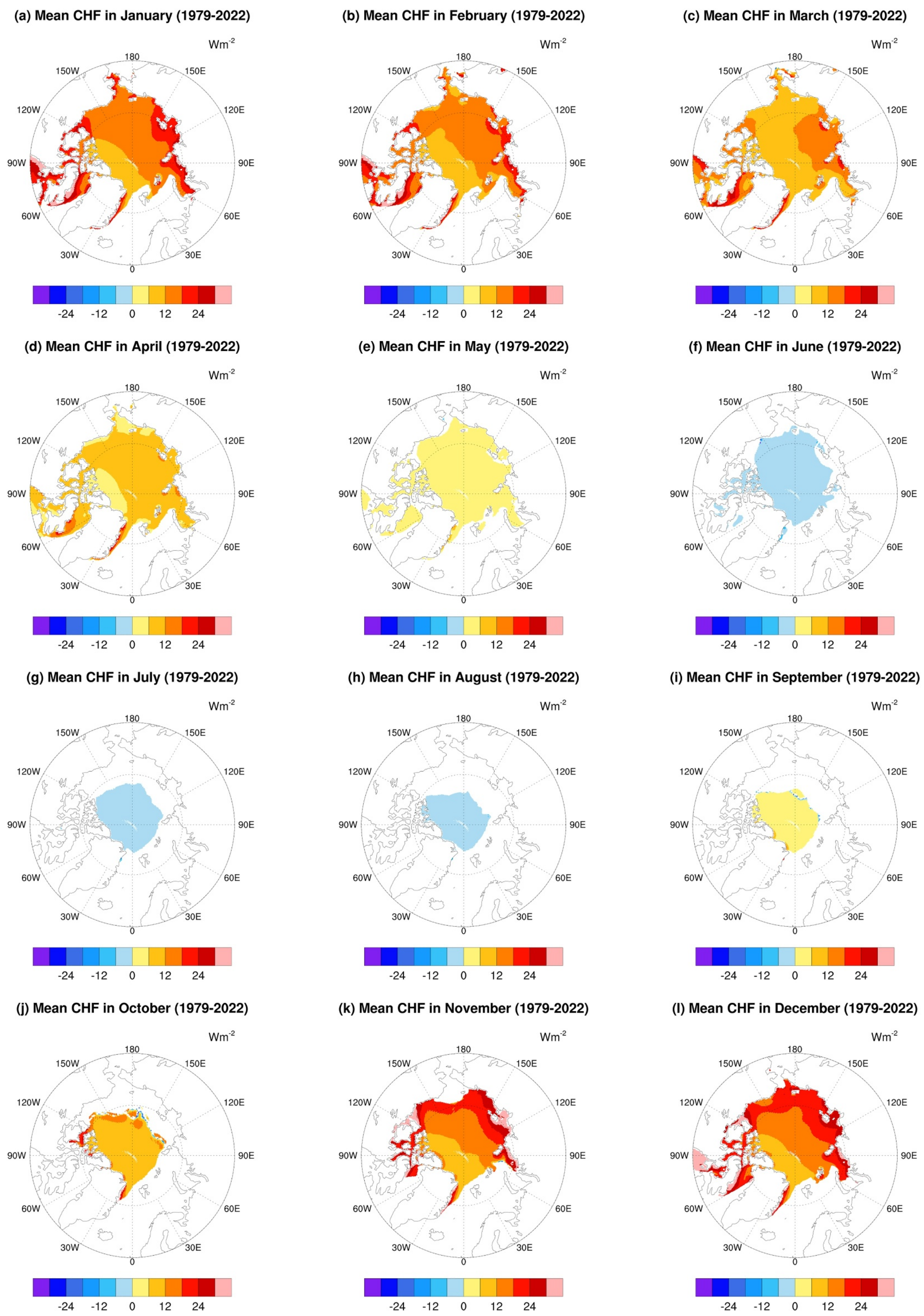


**Figure 3.** Monthly mean conductive heat flux from 1979 to 2022. Only regions with monthly mean sea ice concentration higher than 80% are shown ($Wm^{-2}$).

series from November to February, which show significant positive changes from 1979 to 2022 with higher positive changes over R3 than R1 (Figure 6). For instance, in January, the pronounced positive changes over these seas align with negative changes in sea ice thickness and snow depth, and moderately positive changes in surface

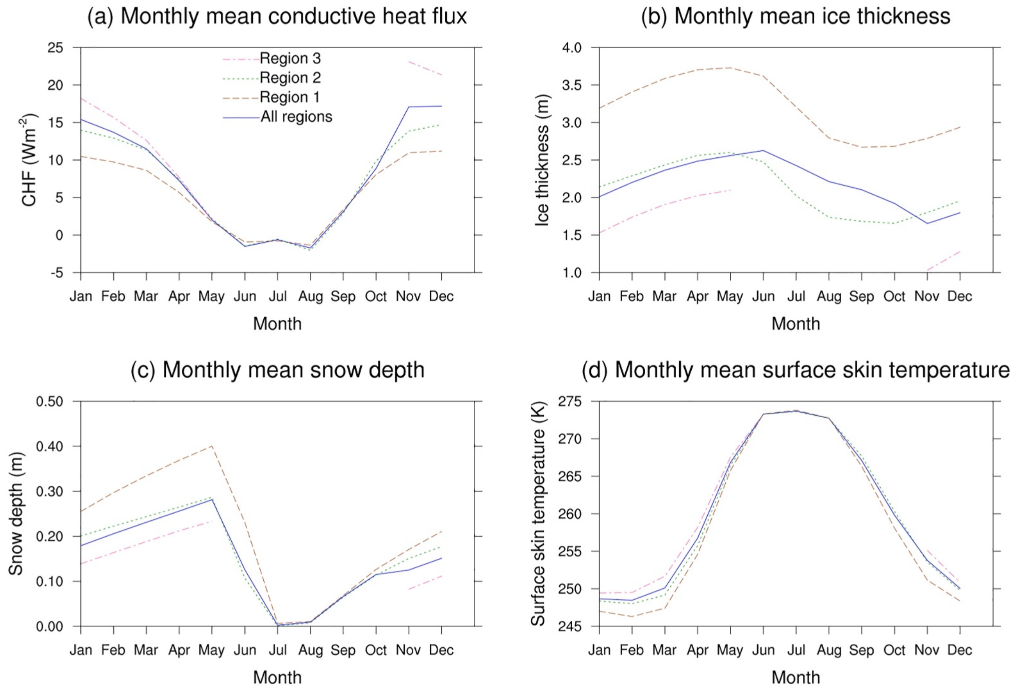


**Figure 4.** Averaged (a) monthly mean conductive heat flux, (b) monthly mean ice thickness, (c) monthly mean snow depth, and (d) monthly mean skin temperature over 3 regions in the Arctic from 1979 to 2022.

skin temperature (Figure 7). Compared to the changes over the Beaufort, Chukchi, and East Siberian Seas, smaller positive changes over the pack ice correlate with larger negative changes in sea ice thickness, modest positive changes in surface skin temperature, and minor negative changes in snow depth; relatively moderate positive changes over the Kara Sea coincide with negative changes in sea ice thickness and snow depth, alongside substantial positive changes in surface skin temperature.

Figure 8 depicts CHF changes attributed to changes in sea ice thickness, snow depth, and surface skin temperature in January, as per Equations 6–8. Positive CHF changes due to changes in sea ice thickness are predominantly observed over peripheral seas as high as 0.24 $Wm^{-2}$/year, driven by large negative changes in sea ice thickness. However, these positive changes diminish north of the Canadian Archipelago, where mean sea ice thickness and snow depth are greater, thereby reducing CHF sensitivity to these changes (Equations 3 and 6). Similarly, positive CHF changes over 0.08 $Wm^{-2}$/year due to changes in snow depth are notable over the peripheral seas, reflecting substantial negative changes in snow depth. Conversely, these positive changes decrease north of the Canadian Archipelago, where less negative snow depth changes and high mean snow depth result in lower CHF sensitivity (Equations 4 and 7). The sensitivity of CHF changes to changes in snow depth is generally higher when all parameters are considered independently, but changes due to changes in sea ice thickness remain comparable or higher, particularly given larger sea ice thickness changes than snow depth and the positive correlations between sea ice thickness and snow depth changes (Equations 6 and 7).

CHF changes attributable to surface skin temperature exhibit predominantly negative values across the Arctic Ocean, reflecting positive changes in surface skin temperature. The absolute values of these changes are less than 0.08 $Wm^{-2}$/year. Notably, more substantial negative changes are observed over the Kara Sea, driven by pronounced warming changes in surface skin temperature, which counterbalance changes from sea ice thickness and snow depth changes and lead to moderately positive CHF changes. Overall, thinner sea ice and snow contribute to stronger CHFs and greater sensitivity of CHF changes to changes in sea ice thickness and snow depth, thereby explaining the largest positive changes and corresponding mean CHFs observed over the Beaufort, Chukchi, and East Siberian Seas in November, December, and January, respectively.

Figure 9 displays spatial averages of changes in CHFs due to changes in sea ice thickness, snow depth, and surface skin temperature. Changes attributed to changes in sea ice thickness closely align with overall CHF changes

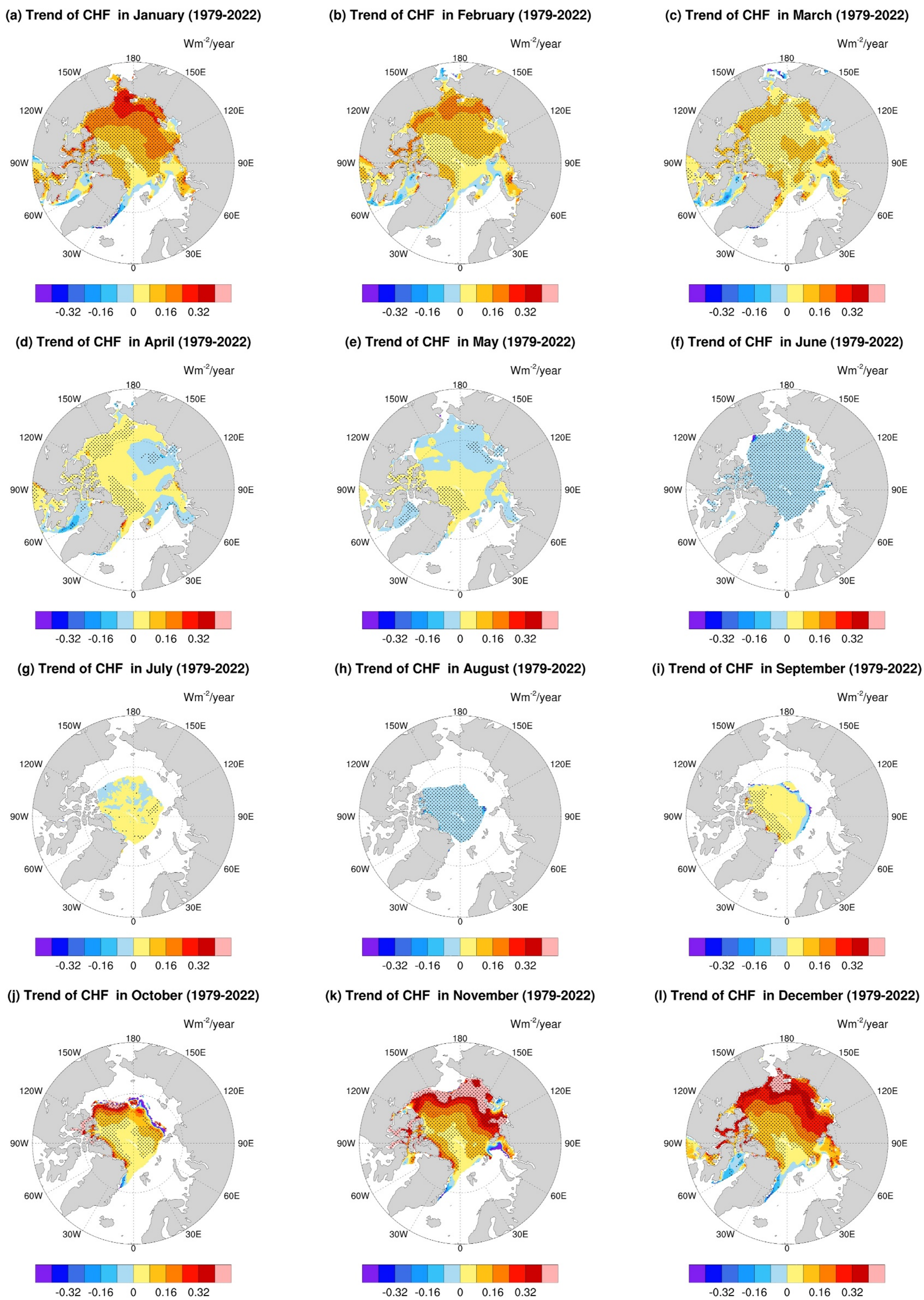


**Figure 5.** Changes of monthly conductive heat flux from 1979 to 2022 (Wm$^{-2}$/year).

across regions R1, R2, and R3. Similarly, changes due to changes in snow depth follow the annual cycle of overall CHF changes, but with a less pronounced variation in magnitude. Conversely, changes due to changes in surface skin temperature exhibit negative values across all regions, opposing the annual cycle of overall CHF changes,

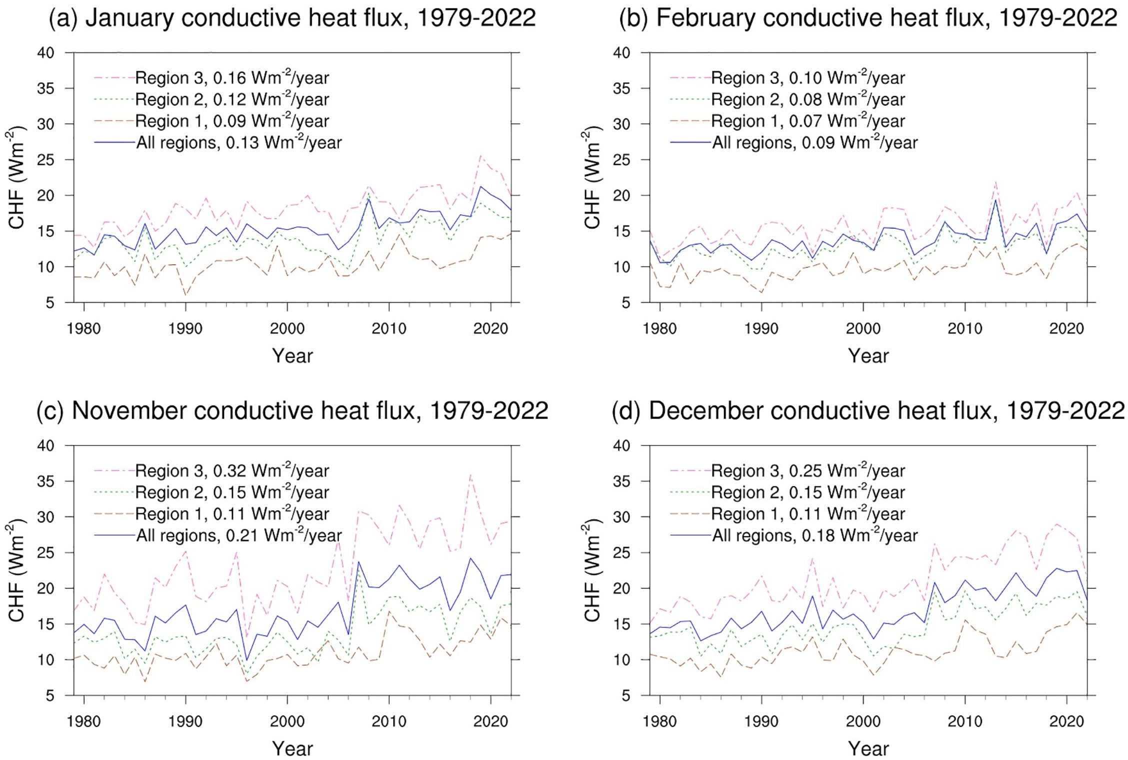


**Figure 6.** Time series of monthly mean CHFs in (a) January, (b) February, (c) November, and (d) December from 1979 to 2022 over region 1, region 2, region 3, and the Arctic Ocean, respectively, as shown in Figure 1. All the changes listed in these figures are statistically significant at the 95% confidence level.

particularly noticeable from November to April. CHF changes due to changes in sea ice thickness and snow depth turn negative when surface skin temperature exceeds the freezing point, despite negative changes in sea ice thickness and snow depth. The sensitivity of CHF changes to changes in sea ice thickness and snow depth is strongest in region R3, followed by R2 and then R1, corresponding to the mean state of sea ice thickness and snow depth in these regions. These results are consistent with those seen in the CHF changes for January (Figure 8).

CHF is a critical component of the surface energy budget, and comparing its seasonal variations and changes with other surface energy fluxes provides valuable insights. The annual evolutions of monthly mean CHF, surface sensible heat flux (SSHF), surface net longwave radiation flux (STR), and surface latent heat flux (SLHF) are shown in Figure 10 to illustrate their variations with season and their relative magnitudes. The STR exhibits negative values in all months (net flux from the surface to the atmosphere) and the largest seasonal variations, with the maximum negative values from December to March around $-40.0\ \mathrm{Wm^{-2}}$ and the minimum negative from July to September around $-16.0\ \mathrm{Wm^{-2}}$. The CHF has comparable magnitude of seasonal variation as that of

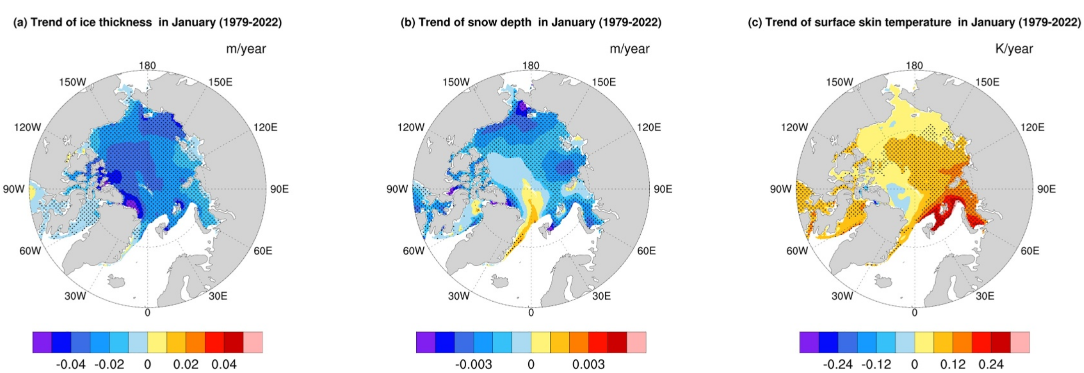


**Figure 7.** Changes of ice thickness (a), snow depth (b), and surface skin temperature (c) in January from 1979 to 2022.

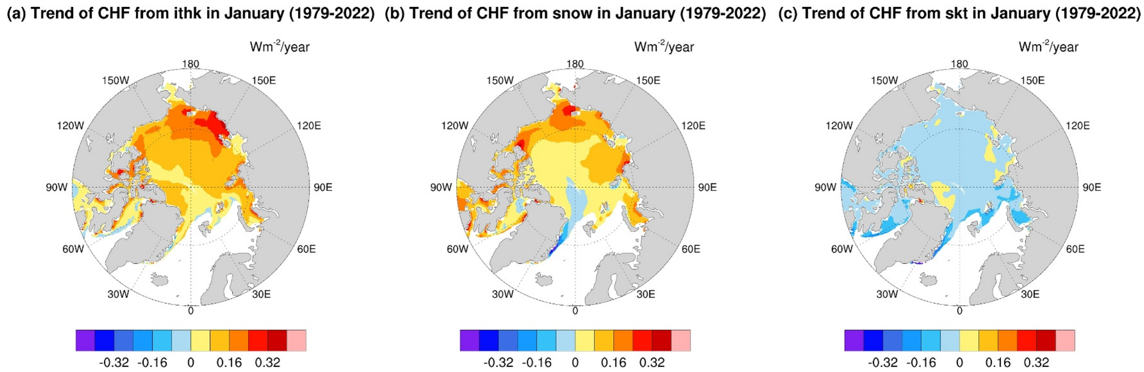


**Figure 8.** Changes of conductive heat flux trend in January from 1979 to 2022 due to (a) trend of ice thickness, (b) trend of snow depth, and (c) trend of surface skin temperature in January from 1979 to 2022.

the STR, with the maximum positive values from November to February around over 10.0 Wm$^{-2}$ over all regions and around 20.0 Wm$^{-2}$ over R3, with the slightly negative values around $-2.0$ Wm$^{-2}$ in August. The SLHF has negative fluxes in all months of a year, with the maximum negative values around $-12.0$ Wm$^{-2}$ in May and June, and the minimum negative values of around $-2.5$ Wm$^{-2}$ from November to March. The SSHF has the smallest seasonal variations, with the maximum negative values of around $-4.0$ Wm$^{-2}$ in November and December over R3 and slightly positive values from June to September.

Figures 5a and 11 illustrates changes in CHF, SSHF, STR, SLHF, and the total of these surface energy flux (STR + SSHF + SLHF; surface solar radiation flux is negligible in January) in January from 1979 to 2022. Positive changes indicate increased energy flux toward the surface. In January, CHF changes are predominantly positive over the Arctic Ocean, with notably higher values over peripheral seas. SSHF, SLHF, and STR changes, however, exhibit different spatial variability. They are generally positive over the perennial ice region (R1),

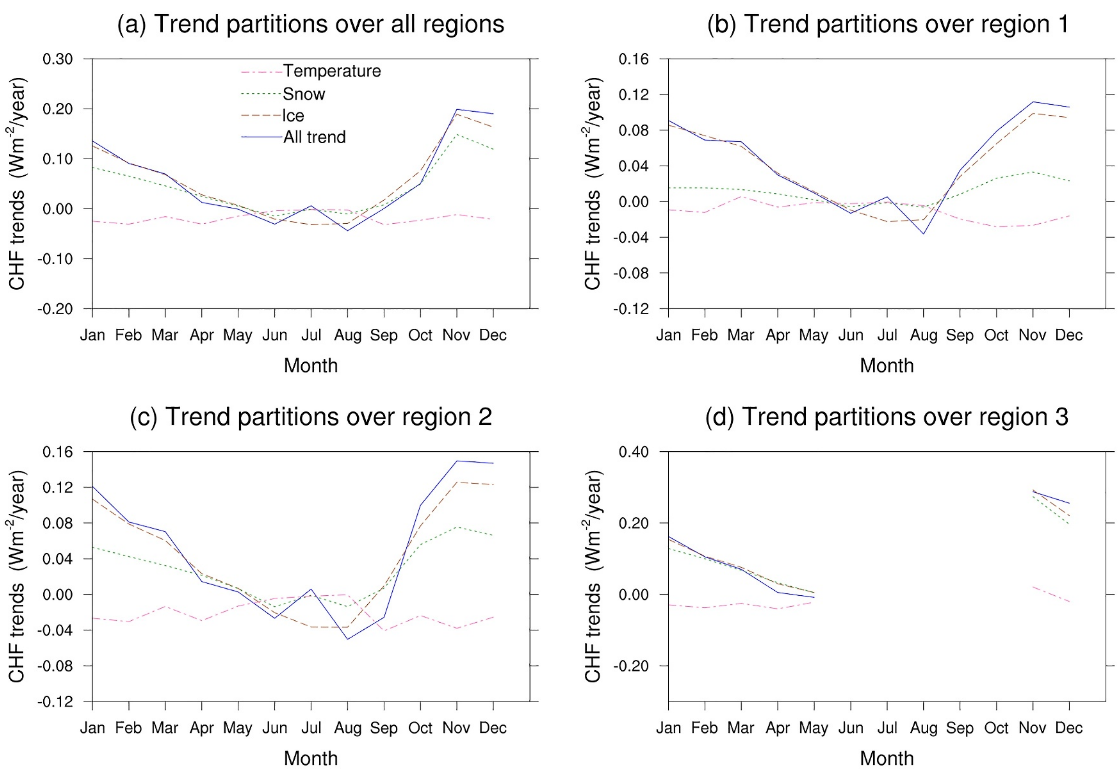


**Figure 9.** Annual conductive heat flux changes and changes due to the changes of ice thickness, snow depth, and surface skin temperature averaged over (a) the Arctic, (b) region 1, (c) region 2, and (d) region 3 shown in Figure 1 from 1979 to 2022.

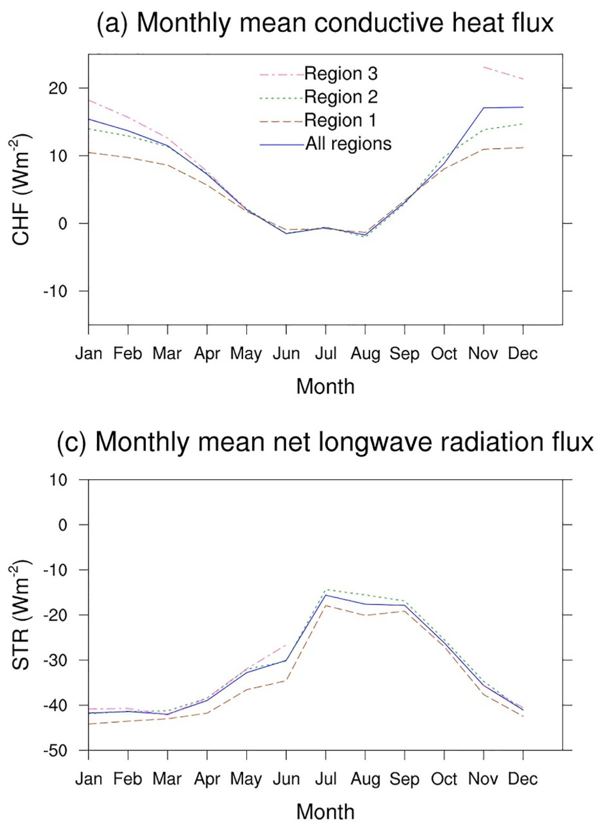


**Figure 10.** Averaged (a) monthly mean conductive heat flux, (b) monthly mean sensible heat flux, (c) monthly mean net longwave radiation flux at the surface, and (d) monthly mean latent heat flux over region 1, region 2, and region 3 as shown in Figure 1, and the Arctic Ocean from 1979 to 2022.

positive with lesser magnitude in the transitional region (R2), and show mixed positive and negative changes over the peripheral seas (R3). The magnitude of CHF changes over peripheral seas is comparable to or higher than the changes observed for SSHF, SLHF, and STR over the pack ice.

Figure 12 presents annual cycles of regional averages of CHF, STR, SSHF, and SLHF changes from 1979 to 2022. Please note our focus is in wintertime, so the SSR term is not included here. In region 1, STR, SSHF, and SLHF changes are positive in most months, with STR showing the highest positive values in most months, for example, close to 0.28 $Wm^{-2}$/year in February. CHF changes are comparable to other flux changes from November to January at around 0.10 $Wm^{-2}$/year but exhibit smaller magnitudes in other months, turning negative from June to August. In region 2, STR, SSHF and SLHF changes are positive in most months, with STR displaying the highest positive values in most months, for example, 0.24 $Wm^{-2}$/year in April. CHF changes align closely with other flux changes from October to March but turn negative from June to August. In region 3, CHF changes are positive from November to March and larger than any other changes, for example, 0.29 $Wm^{-2}$/year in November, and display comparable magnitudes with other flux changes from March to May. SSHF and SLHF changes, however, are negative from November to January.

## 4. Discussion

CHF changes depend on changes in sea ice thickness and snow depth. Positive CHF changes can be attributed to negative changes in ice thickness and snow depth, as well as negative changes in surface skin temperature. Over the past few decades, with the reduction in sea ice thickness, CHFs have increased, especially over the peripheral seas from November to March. The increased CHFs toward the surface are expected to warm the surface, resulting in higher surface temperatures. Many processes contribute to polar amplification (P. C. Taylor et al., 2022), and the increase in CHFs can be one of these processes. Meanwhile, other energy flux terms at the surface are also changing due to various processes. For example, moisture transport and warm air advection into the Arctic warm and moisten the air, potentially producing more clouds, and leading to positive changes in

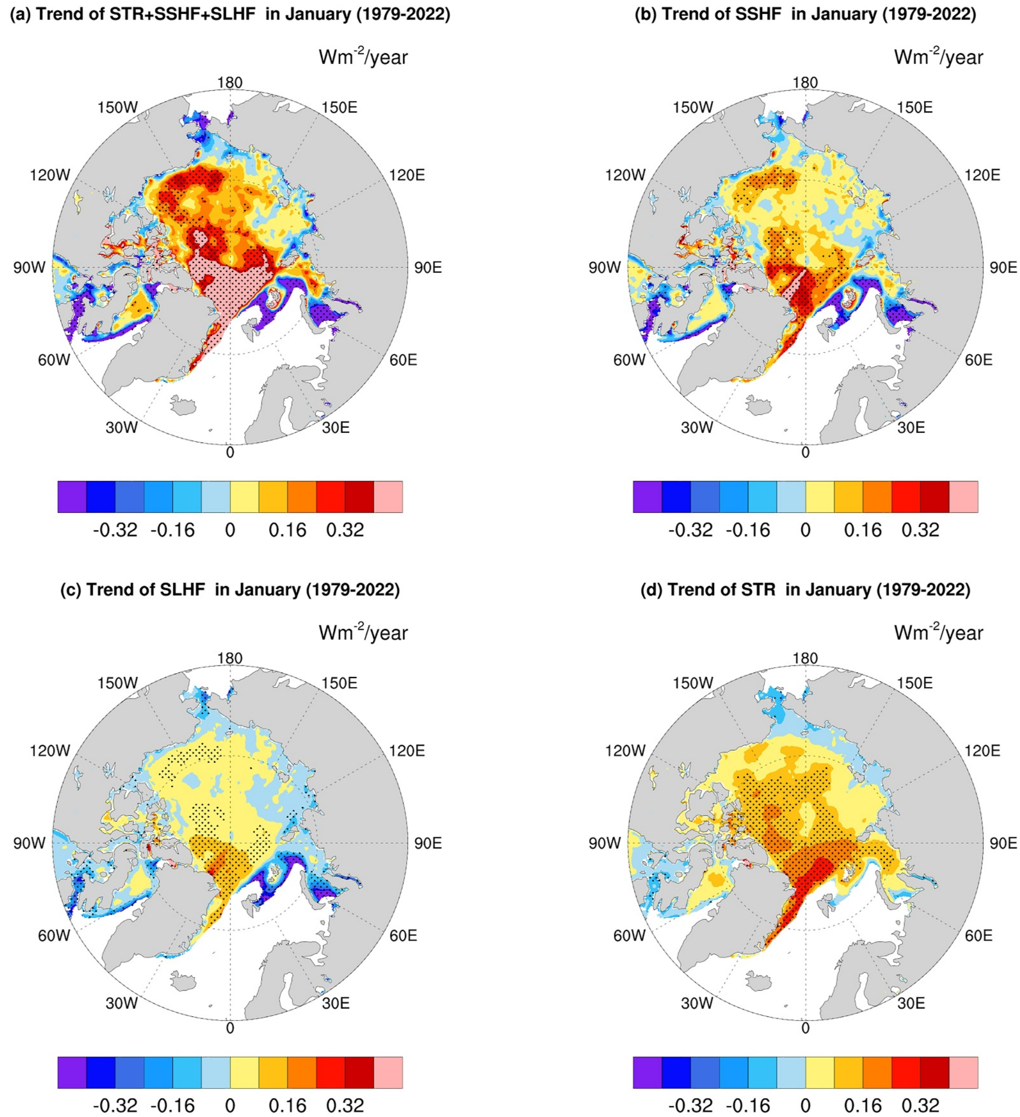


**Figure 11.** (a) Trend of total of surface net longwave radiation flux (STR), surface sensible heat flux (SSHF), and surface latent heat flux (SLHF), (b) trend of SSHF, (c) trend of SLHF, and (d) trend of STR in January from 1979 to 2022. Vertical fluxes are positive toward the surface.

downward longwave radiation (Liu et al., 2018; Park et al., 2015). The positive changes in CHFs from November to March indicate increased latent heat of fusion from sea ice growth, leading to stronger sea ice growth during these months. This suggests that this process helps sea ice thickness recover after dramatic reductions. However, the monthly mean sea ice thickness continues to decrease across the entire Arctic Ocean from 1979 to 2022, indicating that many other processes play a role. These include the sea ice albedo feedback in the summer, moisture intrusion, heat advection into the Arctic in the winter, stronger ocean heat transport, and many other processes that may contribute to sea ice melt in the Arctic (P. C. Taylor et al., 2022).

Monthly mean data were utilized instead of daily data for CHF calculations, which introduces potential uncertainties. For January 2001, the monthly mean CHF was computed as the average of daily CHFs derived from daily sea ice thickness, snow depth, and surface skin temperature. Comparing both CHFs (Figures 2a and A2a) for January 2001 reveals a bias of 0.13 $Wm^{-2}$ and a root mean square error (RMSE) of 0.76 $Wm^{-2}$, with a spatial average of 15.1 $Wm^{-2}$. Despite this uncertainty, it is unlikely to significantly impact the primary conclusions drawn in this study. Arctic sea ice extent reached record lows in 2007 and 2012. To assess the impact of extreme conditions on the CHF uncertainties, similar analyses were performed for January 2008 and 2013, comparing

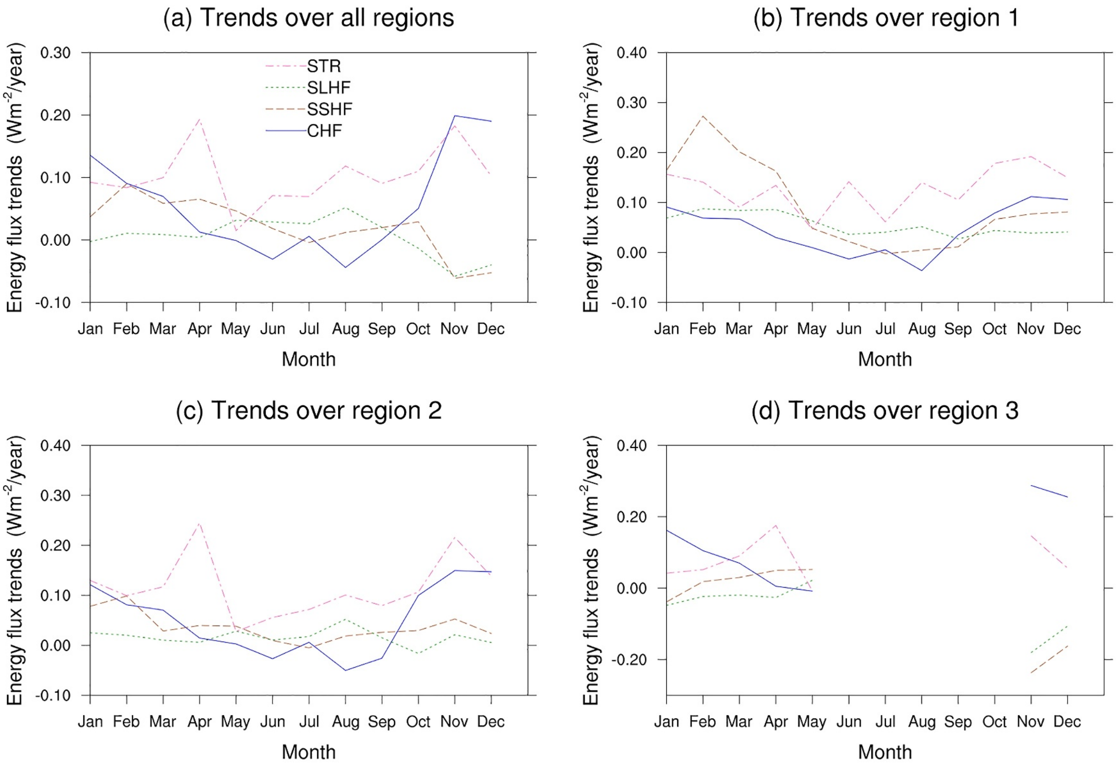


**Figure 12.** Trend of conductive heat flux (CHF), the surface sensible heat flux (SSHF), surface latent heat flux (SLHF), and surface net longwave radiation flux (STR) averaged over (a) the Arctic, (b) region 1, (c) region 2, and (d) region 3, respectively, shown in Figure 1 from 1979 to 2022.

CHFs derived from monthly mean data to those from daily data. The resulting biases were −1.07 and −0.52 $Wm^{-2}$, with RMSEs of 0.75 and 1.11 $Wm^{-2}$, corresponding to spatial averages of 18.7 and 17.5 $Wm^{-2}$, respectively. It is also worth noting that extreme events, such as storms, and their effects on ice thickness and snow depth are well represented in PIOMAS (Zhang et al., 2013).

PIOMAS ice thickness has been validated against in situ ice thickness measurements from submarines, ICESat retrieved ice thickness, and model ice thickness (Schweiger et al., 2011). The results indicate that PIOMAS ice thickness has an uncertainty of 0.78 m (RMS), with biases up to 0.4 m when compared to submarine measurements. However, PIOMAS tends to overestimate thin ice thickness and underestimate thick ice, potentially leading to a smaller decreasing trend in ice volume than reconstructions based on observations. PIOMAS ice thickness agrees well with ICESat ice thickness retrievals, with a mean difference of less than 0.1 m over areas where submarine data are available, although differences are larger outside these areas. Spatial patterns of PIOMAS thickness closely resemble those of ICESat thickness, with pattern correlations exceeding 0.8. The uncertainties in PIOMAS sea ice thickness can affect the derived means and changes of CHF, as well as the distribution of CHF changes attributed to changes in sea ice thickness, snow depth, and surface temperature. The uncertainties in PIOMAS snow depth have been less extensively studied compared to sea ice thickness. PIOMAS snow depth has been evaluated against snow depth data from Operation IceBridge's airborne measurements, ice mass balance snow buoys, and satellite retrievals from Ka-band frequency SARAL/Altika and Ku-band frequency CryoSat-2 in the Arctic (Garnier et al., 2021). The results indicate that PIOMAS snow depth exhibits similar spatial distribution and pan-Arctic mean values to satellite retrievals, albeit with higher overall values. When compared to Operation IceBridge data from 2014 to 2018, PIOMAS shows a bias of 4.3 cm and an RMSE of 10.2 cm. Comparisons with ice mass balance snow buoys from 2013 to 2016 reveal a bias of −2.2 cm and an RMSE of 5.11 cm (Garnier et al., 2021). These uncertainties in PIOMAS snow depth may also contribute to uncertainties in CHF calculations. Comparison of ERA5 reanalysis to buoy observations in the Arctic from 2011 to 2020 shows that ERA5 surface temperature has a cold bias of −4.11°C with an uncertainty of 3.92°C (Yu et al., 2021). ERA5 ice surface temperature is shown to have a warm bias in the Antarctic when satellite derived ice surface temperature products are used as a reference without uncertainty information provided (Wang et al., 2024).

According to J. R. Taylor (1982), the uncertainty in the CHF resulting from uncertainties in PIOMAS snow depth, ice thickness, and ERA5 surface temperature can be estimated using uncertainty propagation. The total CHF uncertainty is calculated as the square root of the sum of the squares of the partial derivatives of CHF with respect to each variable, each multiplied by the uncertainty in that variable. For example, with a sea ice thickness of 2.0 m, snow depth of 0.2 m, and surface skin temperature of 251.0 K, the CHF is 12.2 $Wm^{-2}$. The partial derivatives of CHF with respect to ice thickness, snow depth, and surface temperature are the $-3.7$ $Wm^{-2}$/m, $-23.8$ $Wm^{-2}$/m, and $-0.6$ $Wm^{-2}$/K, respectively as in Section 2.1. Given uncertainties of 0.78 m for ice thickness, 0.102 m for snow depth, and 3.92 K for surface temperature, the resulting overall CHF uncertainty is approximately 4.4 $Wm^{-2}$.

The CHF calculation simplifies by assuming a linear vertical temperature distribution within the snow and sea ice. However, in reality, this process is more complex. Assuming a linear vertical temperature profile in the ice slab results in a uniform conductive heat flux across the ice slab, which can influence estimates of ice thickness. Comparisons of annual mean ice thickness between the three-layer model, which incorporates a nonlinear vertical temperature profile, and the zero-layer model with a linear vertical temperature profile reveal differences. For example, with a mean ice thickness of 2.52 m, the discrepancy is 0.07 m or 3% (Wang et al., 2010; Zhang and Rothrock, 2001).

In the wintertime, the positive CHF changes are larger than the total of other energy flux changes over the peripheral seas (Figure A3), especially from November to February (Figure A3d). Spatially, the CHF changes show positive changes over Barents, Chukchi, and East Siberia Seas from November to February (Figure 5). In ERA5, the sea thickness is set as uniform and constant at 1.5 m, and ERA5 does not apply an explicit prognostic parameterization of the snow cover (Batrak et al., 2024). It is expected that derived CHF based on ERA5 ice thickness and snow depth over sea ice would not show strong positive CHF over the peripheral seas. One possible impact might be underestimate of the surface temperature warming changes over the peripheral seas, as the surface skin temperature trend in January shown in Figure 6c.

## 5. Conclusions

The CHF is a crucial component of the surface energy budget over the Arctic Ocean, closely tied to sea ice growth and influencing surface temperatures. This study calculated monthly mean CHFs from 1979 to 2022 using sea ice thickness and snow depth data from PIOMAS reanalysis, along with surface skin temperature data from ERA5 reanalysis. Monthly CHF means and changes in monthly CHF over the study period were computed and presented. Given that CHF depends on sea ice thickness, snow depth, and surface skin temperature, the study also analyzed changes in CHF attributable to changes in these variables. Comparisons were made between CHF changes and those of surface sensible heat flux (SSHF), surface latent heat flux (SLHF), and surface net radiation flux (STR). Spatial averages of these variables and their changes were calculated across perennial ice areas, coastal areas, and transitional zones. Key findings include the following:

- Spatially, over the Arctic Ocean, the highest CHFs are observed over coastal areas and peripheral seas where sea ice thickness and snow depth are minimal. CHF values decrease toward the pack ice regions and reach their minimum near the regions north of the Canadian Archipelago and Greenland. Seasonally, the maximum positive CHFs occur in November and December, coinciding with the beginning of the sea ice growth after the melting season. CHF gradually decreases from January to May, reaching negative values from June to August. CHF returns to positive values in September and continues to increase thereafter.
- Changes of monthly CHFs from 1979 to 2022 show predominantly positive values over the Arctic Ocean from October to March, with negative changes in June and August. The largest positive changes are observed over the Beaufort, Chukchi, and East Siberian Seas in November, December, and January, respectively, coinciding with the highest mean CHFs during those months.
- The changes of CHFs due to changes in sea ice thickness, snow depth, and surface skin temperature are predominantly positive, positive, and negative, respectively. The overall trend of CHF averaged over the Arctic Ocean is largely influenced by changes in sea ice thickness changes.

- The magnitude of the CHF changes is comparable to the changes of surface sensible heat flux (SSHF), surface latent heat flux (SLHF), and surface net longwave/thermal radiation flux (STR) over the pack ice. Changes in CHF over the peripheral seas may exceed those of SSHF, SLHF, and STR.
- A better representation of sea ice thickness and snow depth over sea ice in the reanalysis would possibly produce realistic CHF changes, and improve the depiction of the surface temperature changes.

This study presents a methodology to calculate CHFs using reanalysis data and potentially satellite retrievals. With available sea ice thickness data from satellite retrievals and the potential for satellite-retrieved snow depth data, monitoring CHFs over the sea ice-covered Arctic Ocean in near real time could enable more accurate estimates of sea ice growth. Given the expected ongoing decrease in Arctic sea ice, with potential summer ice-free conditions projected for this century (Diebold et al., 2023; Wang et al., 2022), monitoring how CHFs would change under this scenario is important and needs further research.

## Appendix A

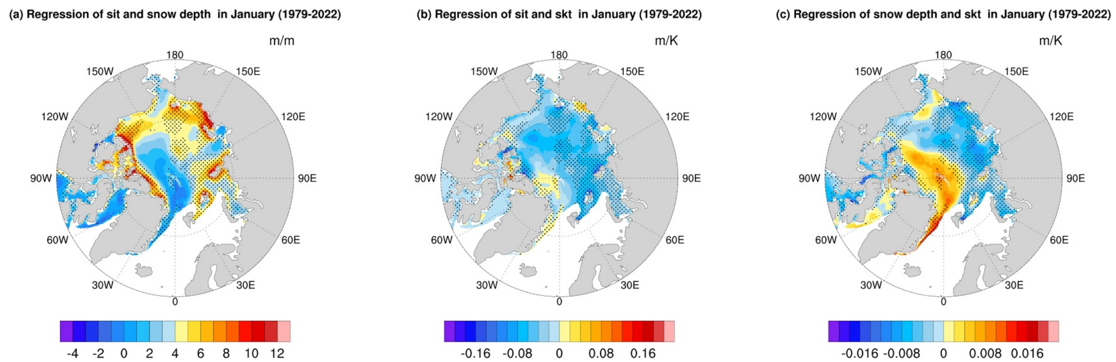


**Figure A1.** Regression coefficients of (a) sea ice thickness (sit) on snow depth, (b) sit on surface skin temperature (skt), and (c) snow depth on skt in January from 1979 to 2022.

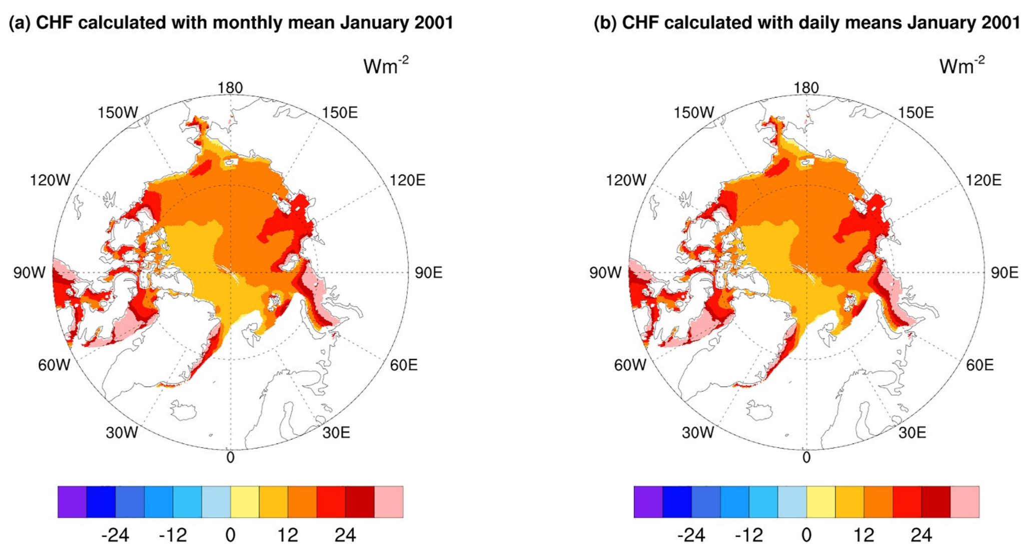


**Figure A2.** Derived conductive heat flux based on (a) monthly mean as in Figure 2a and (b) mean of the daily conductive heat fluxes from daily mean sea ice thickness, snow depth, and surface skin temperature.

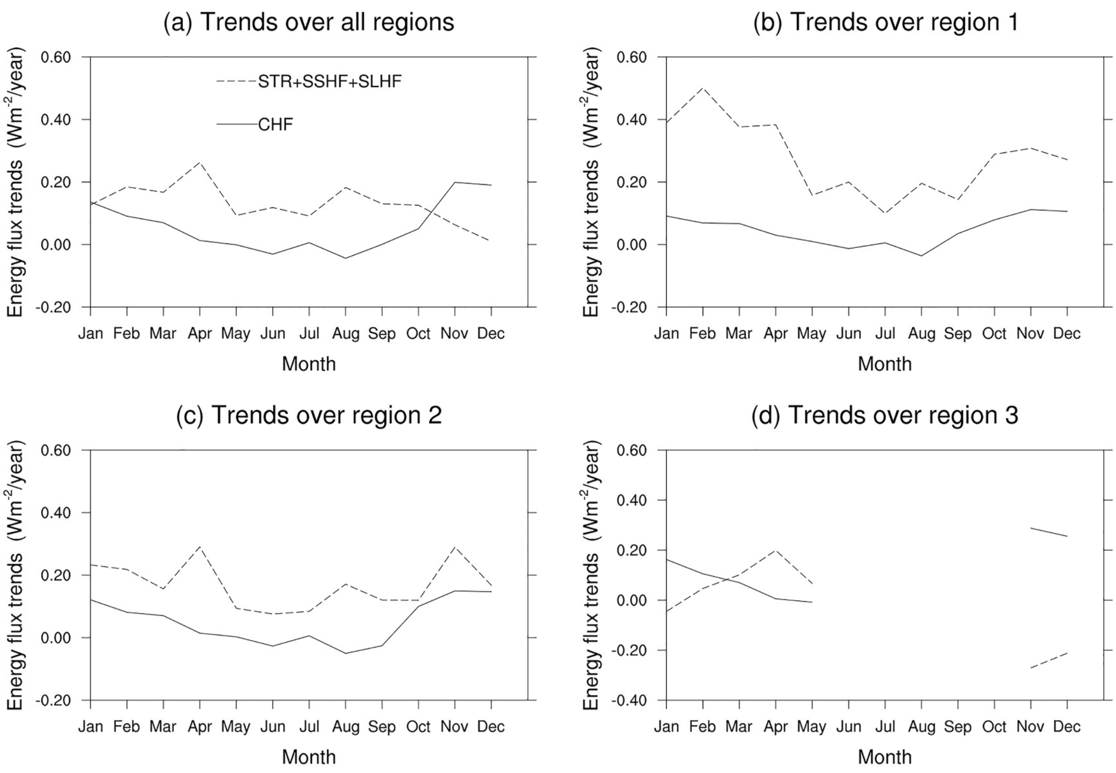


**Figure A3.** Trend of conductive heat flux (CHF), the total of surface sensible heat flux (SSHF), surface latent heat flux (SLHF), and surface net longwave radiation flux (STR) averaged over (a) the Arctic, (b) region 1, (c) region 2, and (d) region 3, respectively, shown in Figure 1 from 1979 to 2022.

## Data Availability Statement

All the PIOMAS reanalysis data used in this study are available at pscfiles.apl.washington.edu:/pscfiles/zhang/PIOMAS/data/v2.1. The ERA5 reanalysis data are available at cds.climate.copernicus.eu and https://doi.org/10.24381/cds.f17050d7. Data analysis were done with code in NCAR Command Language and IDL. All data and code in this study is available at https://doi.org/10.5281/zenodo.15499078 (Liu, 2025).

**Acknowledgments**

This work has been supported by the NOAA JPSS Program Office and GOES-R Series Program Office. The views, opinions, and findings contained in this report are those of the author and should not be construed as an official National Oceanic and Atmospheric Administration or U.S. Government position, policy, or decision. JZ is supported by NASA Cryosphere Program (80NSSC20K1253), ONR (N00014-17-1-3162), and NSF Office of Polar Programs (NNA-1927785).

## References

Anheuser, J., Liu, Y., & Key, J. R. (2022). A simple model for daily basin-wide thermodynamic sea ice thickness growth retrieval. *The Cryosphere*, *16*(10), 4403–4421. https://doi.org/10.5194/tc-16-4403-2022

Arduini, G., Keeley, S., Day, J. J., Sandu, I., Zampieri, L., & Balsamo, G. (2022). On the importance of representing snow over sea-ice for simulating the Arctic boundary layer. *Journal of Advances in Modeling Earth Systems*, *14*(7), e2021MS002777. https://doi.org/10.1029/2021MS002777

Batrak, Y., Cheng, B., & Kallio-Myers, V. (2024). Sea ice cover in the Copernicus Arctic regional reanalysis. *The Cryosphere*, *18*(3), 1157–1183. https://doi.org/10.5194/tc-18-1157-2024

Chylek, P., Folland, C., Klett, J. D., Wang, M., Hengartner, N., Lesins, G., & Dubey, M. K. (2022). Annual mean Arctic amplification 1970–2020: Observed and simulated by CMIP6 climate models. *Geophysical Research Letters*, *49*(13), e2022GL099371. https://doi.org/10.1029/2022GL099371

Connor, L. N., Laxon, S. W., Ridout, A. L., Krabill, W. B., & McAdoo, D. C. (2009). Comparison of Envisat radar and airborne laser altimeter measurements over Arctic sea ice. *Remote Sensing of Environment*, *113*(3), 563–570. https://doi.org/10.1016/j.rse.2008.10.015

Diebold, F. X., Rudebusch, G. D., Göbel, M., Goulet Coulombe, P., & Zhang, B. (2023). When will Arctic sea ice disappear? Projections of area, extent, thickness, and volume. *Journal of Econometrics*, *236*(2), 105479. https://doi.org/10.1016/j.jeconom.2023.105479

Garnier, F., Fleury, S., Garric, G., Bouffard, J., Tsamados, M., Laforge, A., et al. (2021). Advances in altimetric snow depth estimates using bi-frequency SARAL and CryoSat-2 Ka–Ku measurements. *The Cryosphere*, *15*(12), 5483–5512. https://doi.org/10.5194/tc-15-5483-2021

Hersbach, H., Bell, B., Berrisford, P., Hirahara, S., Horányi, A., Muñoz-Sabater, J., et al. (2020). The ERA5 global reanalysis. *Quarterly Journal of the Royal Meteorological Society*, *146*(730), 1999–2049. https://doi.org/10.1002/qj.3803

Holland, M. M., Clemens-Sewall, D., Landrum, L., Light, B., Perovich, D., Polashenski, C., et al. (2021). The influence of snow on sea ice as assessed from simulations of CESM2. *The Cryosphere*, *15*(10), 4981–4998. https://doi.org/10.5194/tc-15-4981-2021

Kwok, R. (2018). Arctic sea ice thickness, volume, and multiyear ice coverage: Losses and coupled variability (1958–2018). *Environmental Research Letters*, *13*(10), 105005. https://doi.org/10.1088/1748-9326/aae3ec

Kwok, R., & Rothrock, D. A. (2009). Decline in Arctic sea ice thickness from submarine and ICESat records: 1958-2008. *Geophysical Research Letters*, *36*(15). https://doi.org/10.1029/2009GL039035

Landrum, L. L., & Holland, M. M. (2022). Influences of changing sea ice and snow thicknesses on simulated Arctic winter heat fluxes. *The Cryosphere*, *16*(4), 1483–1495. https://doi.org/10.5194/tc-16-1483-2022

Lawrence, I. R., Tsamados, M. C., Stroeve, J. C., Armitage, T. W. K., & Ridout, A. L. (2018). Estimating snow depth over Arctic sea ice from calibrated dual-frequency radar freeboards. *The Cryosphere*, *12*(11), 3551–3564. https://doi.org/10.5194/tc-12-3551-2018

Laxon, S. W., Giles, K. A., Ridout, A. L., Wingham, D. J., Willatt, R., Cullen, R., et al. (2013). CryoSat-2 estimates of Arctic sea ice thickness and volume. *Geophysical Research Letters*, *40*(4), 732–737. https://doi.org/10.1002/grl.50193

Lee, S. M., Shi, H., Sohn, B. J., Gasiewski, A. J., Meier, W. N., & Dybkjær, G. (2021). Winter snow depth on Arctic Sea Ice from satellite radiometer measurements (2003–2020): Regional patterns and trends. *Geophysical Research Letters*, *48*(15), e2021GL094541. https://doi.org/10.1029/2021GL094541

Lindsay, R. W., & Zhang, J. (2006). Assimilation of ice concentration in an ice-ocean model. *Journal of Atmospheric and Oceanic Technology*, *23*(5), 742–749. https://doi.org/10.1175/JTECH1871.1

Liu, Y. (2025). Conductive heat flux over Arctic Sea Ice from 1979 to 2022: Data and code [Dataset]. *Zenodo*. https://doi.org/10.5281/zenodo.15499078

Liu, Y., Key, J. R., Vavrus, S., & Woods, C. (2018). Time evolution of the cloud response to moisture intrusions into the Arctic during winter. *Journal of Climate*, *31*(22), 9389–9405. https://doi.org/10.1175/JCLI-D-17-0896.1

Liu, Y., Key, J. R., Wang, X., & Tschudi, M. (2020). Multidecadal Arctic sea ice thickness and volume derived from ice age. *The Cryosphere*, *14*(4), 1325–1345. https://doi.org/10.5194/tc-14-1325-2020

Maslanik, J., Stroeve, J., Fowler, C., & Emery, W. (2011). Distribution and trends in Arctic sea ice age through spring 2011. *Geophysical Research Letters*, *38*(13), L13502. https://doi.org/10.1029/2011GL047735

Maslanik, J. A., Fowler, C., Stroeve, J., Drobot, S., Zwally, J., Yi, D., & Emery, W. (2007). A younger, thinner Arctic ice cover: Increased potential for rapid, extensive sea-ice loss. *Geophysical Research Letters*, *34*(24), L24501. https://doi.org/10.1029/2007GL032043

Moon, T. A., Thoman, R., Druckenmiller, M. L., Ahmasuk, B., Backensto, S. A., Ballinger, T. J., & Veasey, S. W. (2023). The Arctic: Permafrost [in "State of the climate in 2022"]. *Bulletin of the American Meteorological Society*, *104*(9). https://doi.org/10.1175/BAMS-D-23-0079.1

Notz, D. (2005). *Thermodynamic and fluid-dynamical processes in sea ice*. PhD thesis. Cambridge University.

Park, D.-S. R., Lee, S., & Feldstein, S. B. (2015). Attribution of the recent winter sea ice decline over the Atlantic sector of the Arctic Ocean. *Journal of Climate*, *28*(10), 4027–4033. https://doi.org/10.1175/jcli-d-15-0042.1

Rantanen, M., Karpechko, A. Y., Lipponen, A., Nordling, K., Hyvärinen, O., Ruosteenoja, K., et al. (2022). The Arctic has warmed nearly four times faster than the globe since 1979. *Communications Earth & Environment*, *3*(1), 168. https://doi.org/10.1038/s43247-022-00498-3

Schweiger, A., Lindsay, R., Zhang, J., Steele, M., Stern, H., & Kwok, R. (2011). Uncertainty in modeled Arctic sea ice volume. *Journal of Geophysical Research*, *116*(9), C00D06. https://doi.org/10.1029/2011JC007084

Semtner, A. J. (1976). A model for the thermodynamic growth of sea ice in numerical investigations of climate. *Journal of Physical Oceanography*, *6*(3), 379–389. https://doi.org/10.1175/1520-0485(1976)006<0379:amfttg>2.0.co;2

Serreze, M. C., Barrett, A. P., Stroeve, J. C., Kindig, D. N., & Holland, M. M. (2009). The emergence of surface-based Arctic amplification. *The Cryosphere*, *3*(1), 11–19. https://doi.org/10.5194/tc-3-11-2009

Shalina, E. V., & Sandven, S. (2018). Snow depth on Arctic sea ice from historical in situ data. *The Cryosphere*, *12*(6), 1867–1886. https://doi.org/10.5194/tc-12-1867-2018

Taylor, J. R. (1982). *An introduction to error analysis*. University Science Books, Mill Valley.

Taylor, P. C., Boeke, R. C., Boisvert, L. N., Feldl, N., Henry, M., Huang, Y., et al. (2022). Process drivers, inter-model spread, and the path forward: A review of amplified Arctic warming. *Frontiers in Earth Science*, *9*. https://doi.org/10.3389/feart.2021.758361

Thorndike, A. S. (1992). A toy model linking atmospheric thermal radiation and sea ice growth. *Journal of Geophysical Research*, *97*(C6), 9401–9410. https://doi.org/10.1029/92jc00695

Wang, X., Key, J. R., & Liu, Y. (2010). A thermodynamic model for estimating sea and lake ice thickness with optical satellite data. *Journal of Geophysical Research*, *115*(12), C12035. https://doi.org/10.1029/2009JC005857

Wang, X., Liu, Y., Key, J. R., & Dworak, R. (2022). A new perspective on four decades of changes in Arctic sea ice from satellite observations. *Remote Sensing*, *14*(8), 1846. https://doi.org/10.3390/rs14081846

Wang, Z., Fraser, A. D., Reid, P., O'Farrell, S., & Coleman, R. (2024). Antarctic sea ice surface temperature bias in atmospheric reanalyses induced by the combined effects of sea ice and clouds. *Communications Earth & Environment*, *5*(1), 552. https://doi.org/10.1038/s43247-024-01692-1

Webster, M. A., Rigor, I. G., Nghiem, S. V., Kurtz, N. T., Farrell, S. L., Perovich, D. K., & Sturm, M. (2014). Interdecadal changes in snow depth on Arctic sea ice. *Journal of Geophysical Research: Oceans*, *119*(8), 5395–5406. https://doi.org/10.1002/2014jc009985

Yu, Y., Xiao, W., Zhang, Z., Cheng, X., Hui, F., & Zhao, J. (2021). Evaluation of 2-m air temperature and surface temperature from ERA5 and ERA-I using buoy observations in the Arctic during 2010–2020. *Remote Sensing*, *13*(14), 2813. https://doi.org/10.3390/rs13142813

Zhang, J., Lindsay, R., Schweiger, A., & Steele, M. (2013). The impact of an intense summer cyclone on 2012 Arctic sea ice retreat. *Geophysical Research Letters*, *40*(4), 720–726. https://doi.org/10.1002/grl.50190

Zhang, J., & Rothrock, D. (2001). A thickness and enthalpy distribution sea-ice model. *Journal of Physical Oceanography*, *31*(10), 2986–3001. https://doi.org/10.1175/1520-0485(2001)031<2986:ATAEDS>2.0.CO;2

Zhang, J., & Rothrock, D. A. (2003). Modeling global sea ice with a thickness and enthalpy distribution model in generalized curvilinear coordinates. *Monthly Weather Review*, *131*(5), 845–861. https://doi.org/10.1175/1520-0493(2003)131<0845:MGSIWA>2.0.CO;2